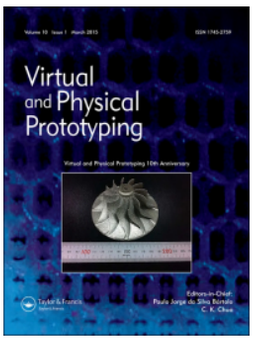

Taylor & Francis
Taylor & Francis Group

Virtual and Physical Prototyping

ISSN: (Print) (Online) Journal homepage: https://www.tandfonline.com/loi/nvpp20

Virtual surface morphology generation of Ti-6Al-4V directed energy deposition via conditional generative adversarial network

Taekyeong Kim, Jung Gi Kim, Sangeun Park, Hyoung Seop Kim, Namhun Kim, Hyunjong Ha, Seung-Kyum Choi, Conrad Tucker, Hyokyung Sung & Im Doo Jung

To cite this article: Taekyeong Kim, Jung Gi Kim, Sangeun Park, Hyoung Seop Kim, Namhun Kim, Hyunjong Ha, Seung-Kyum Choi, Conrad Tucker, Hyokyung Sung & Im Doo Jung (2023) Virtual surface morphology generation of Ti-6Al-4V directed energy deposition via conditional generative adversarial network, Virtual and Physical Prototyping, 18:1, e2124921, DOI: 10.1080/17452759.2022.2124921

To link to this article: https://doi.org/10.1080/17452759.2022.2124921

VIRTUAL AND PHYSICAL PROTOTYPING
2022, VOL. 18, NO. 1, e2124921 (17)
https://doi.org/10.1080/17452759.2022.2124921

Virtual surface morphology generation of Ti-6Al-4V directed energy deposition via conditional generative adversarial network

Taekyeong Kim [a]*, Jung Gi Kim [b]*, Sangeun Park [b], Hyoung Seop Kim [c], Namhun Kim [a], Hyunjong Ha [d], Seung-Kyum Choi [e], Conrad Tucker [f], Hyokyung Sung [b,g] and Im Doo Jung [a]

[a]Department of Mechanical Engineering, Ulsan National Institute of Science and Technology, Ulsan, Republic of Korea; [b]Department of Materials Engineering and Convergence Technology (Center for K-Metals), Gyeongsang National University, Jinju, Republic of Korea; [c]Department of Materials Science and Engineering, Center for High-Entropy Alloys, Pohang University of Science and Technology, Pohang, Republic of Korea; [d]Korea Institute of Materials Science, Changwon, Republic of Korea; [e]The George W. Woodruf School of Mechanical Engineering, Georgia Institute of Technology, Atlanta, GA, USA; [f]Department of Mechanical Engineering, Carnegie Mellon University, Pittsburgh, PA, USA; [g]Department of Materials Science and Engineering, Kookmin University, Seoul, Republic of Korea

ABSTRACT

The core challenge in directed energy deposition is to obtain high surface quality through process optimisation, which directly affects the mechanical properties of fabricated parts. However, for expensive materials like Ti-6Al-4V, the cost and time required to optimise process parameters can be excessive in inducing good surface quality. To mitigate these challenges, we propose a novel method with artificial intelligence to generate virtual surface morphology of Ti-6Al-4V parts by given process parameters. A high-resolution surface morphology image generation system has been developed by optimising conditional generative adversarial networks. The developed virtual surface matches experimental cases well with an Fréchet inception distance score of 174, in the range of accurate matching. Microstructural analysis with parts fabricated with artificial intelligence guidance exhibited less textured microstructural behaviour on the surface which reduces the anisotropy in the columnar structure. This artificial intelligence guidance of virtual surface morphology can help to obtain high-quality parts cost-effectively.

ARTICLE HISTORY
Received 20 July 2022
Accepted 11 September 2022

KEYWORDS
Directed energy deposition; surface morphology; Ti-6Al-4V; artificial intelligence; conditional generative adversarial network; columnar structure

1. Introduction

Directed energy deposition (DED), the process of depositing powder through a nozzle and melting it with a laser, is one of the most adaptable additive manufacturing (AM) methods to date, primarily because of its capability to consolidate large size complex shape components in a layer-by-layer fabrication. DED is also useful for the repair of components in the aerospace (Gradl 2021; Blakey-Milner et al. 2021), biomedical (Amato et al. 2013), and automotive industries (Bennett et al. 2019).

The DED fabrication process consists of powder feeding, laser melting, fusion, and the solidification of layers. As mechanical properties and microstructures of fabricated parts are significantly influenced by the processing parameters, there have been many studies to improve tensile properties and elongation via process optimisation. The relationship between the characterisation of stainless steel, scan speed, and laser power was investigated (Zhang et al. 2014). The effect of laser power and powder feed rate on the porosity of Ti–6Al–4V structures were also examined (Qiu et al. 2015). The dwell time (Denlinger et al. 2015), hatch spacing (Wang et al. 2019), scanning pattern (Zhang et al. 2021; Dharmawan and Soh 2022; Jhabvala et al. 2010), laser incident energy (Xue et al. 2021), powder morphology (Ang et al. 2022; Farzaneh et al. 2022), and layer thickness (Shim et al. 2016) can critically affect the mechanical properties and quality of AM. The relationship between the hatch rotation angle and build quality was investigated (Terrassa et al. 2019). The ultrasonic vibration-assisted DED was also conducted to reduce defects due to lamination, resulting in the refining of microstructure and improving characterisation of stainless steel (Yang et al. 2022, 2021).

However, despite the rapid progress of mechanical strength, DED still has a bottleneck, in that, the surface quality is lower than that of other methods such as

CONTACT Hyokyung Sung hyokyung@kookmin.ac.kr Kookmin University, Seoul 02707, Republic of Korea; Im Doo Jung idjung@unist.ac.kr Ulsan National Institute of Science and Technology, Ulsan 44919, Republic of Korea
*These authors contributed equally to this work.
Supplemental data for this article can be accessed online at https://doi.org/10.1080/17452759.2022.2124921.

laser powder bed fusion (L-PBF) (Barroqueiro et al. 2019; Alex Huckstepp 2019). This is primarily caused by the relatively larger powder size used in DED (D50, 60 µm ~ 100 µm) compared to the laser PBF (D50, 30 µm ~ 45 µm) resulting in slow melting (Doñate-Buendia et al. 2021). In particular, the surface roughness of DED is high because the deposition rate is higher, and the size of the melt pool is larger than other AM processes (Udroiu, Braga, and Nedelcu 2019; Dutta 2020). Surface roughness also critically affects the fatigue property, as a poor surface can induce crack initiation at the surface under repetitive external forces (Wang et al. 2019; Jingzhe Zhang and Fatemi 2019). These limitations require additional post-processing tasks (Lee, Nagalingam, and Yeo 2021) and restrict the widespread application of DED in manufacturing products in various industries.

To address this issue, there have been several experimental efforts to optimise DED process parameters to control surface quality and bead appearance which is related to surface roughness (Udroiu, Braga, and Nedelcu 2019) and welding defects and bead shape (Nam et al. 2018). A correlation between periodic meniscus and the melt-pool geometry was established (Gharbi et al. 2013). The ultrasonic method was applied to determine the effect of process parameters on surface porosity (Rao et al. 2022). However, these experimental approaches can be costly for expensive materials such as Ti-6Al-4V to find optimum conditions for the fabrication of each part.

Recently, artificial intelligence (AI) has been actively employed in AM, which is a reliable and fast way to predict and optimise processing parameters. For example, artificial neural network (ANN) application to metal was studied to determine weld geometry and temperature distribution (Akbari et al. 2016). A comparative study on predicting the thermal history in DED was performed using a recurrent neural network (Mozaffar et al. 2018). An ANN was also employed to define the correlation between process parameters and geometrical parameters, such as the width, height, and depth of the deposited trace (Caiazzo and Caggiano 2018). Bead shapes and porosity formation in the processed DED part have also been studied (Wacker et al. 2021; Liu, Liu, and Zhang 2021; Mbodj et al. 2021). Furthermore, neural network studies have also been conducted to predict the deposition shape of the wire arc AM by analysing the correlation between the deposition shape and process conditions such as bead width and height (Xiao et al. 2022). A long short-term memory was employed to predict the tensile strength of the printed parts using the fused deposition modelling (Zhang, Wang, and Gao 2018). However, most of these AI applications were focused on increasing mechanical properties via process optimisation, which still requires further studies on DED surface quality improvement affecting fatigue behaviour.

In this work, a novel method is developed for quick prediction of the surface morphology of the metal DED surface via a conditional generative adversarial network (CGAN). Through CGAN structure optimisation with initial experimental data, the virtual graphic generation model was developed to predict the surface morphology of the DED parts based on any desired process input. With the CGAN virtual guidance, the Ti-6Al-4V part was fabricated and analysed via microstructural studies.

2. Materials & methods

2.1 Experimental setup

As shown in Table 1, the Ti–6Al–4V powder of MK Corporation was used for the DED process, and the proportions of the components are listed. Powder morphology can be found in Figure 1(a). The particle size distribution is 62.73 µm for d10, 92.41 µm for d50, and 144.70 µm for d90, which are larger than the average powder size used in L-PBF as shown in Figure 1(b), and the average tap density of the powder is 2.55 g/cm^3.

InssTek MX-Lab, which is equipped with an ytterbium fibre laser with an output of up to 300 W, was used for the DED process along with a clogged vibration method, in which the powder is supplied to the nozzle using the vertical vibration of the feeder. The tool path was moved along the track in a contour (clockwise)–filling (zigzag)–contour (counterclockwise) sequence for each layer, with two outer construction processes (Figure 2). The pattern was rotated 90° clockwise whenever each layer was completed.

Cuboids with dimensions of 12 mm × 18 mm × 12 mm (length × width × height), having 80 layers 0.15 mm high, were manufactured on a plate. The variables of the process conditions shown in Table 2, consist of three components: laser power (160–220 W), powder feed rate (0.4–0.7 g/min), and scanning speed (850–1000 mm/min) each with values within a specified range, and its list is shown in Table S1.

The top surface of the cuboid was scanned with ATOS CORE 45 from GOM where each of the three sensors performed a scan at a different angle, producing two-dimensional (2D) and three-dimensional (3D) scan

Table 1. Chemical composition of the Ti–6Al–4V powder.

Element	Ti	Al	V	Fe
wt%	Bal.	6.36	4.06	0.18

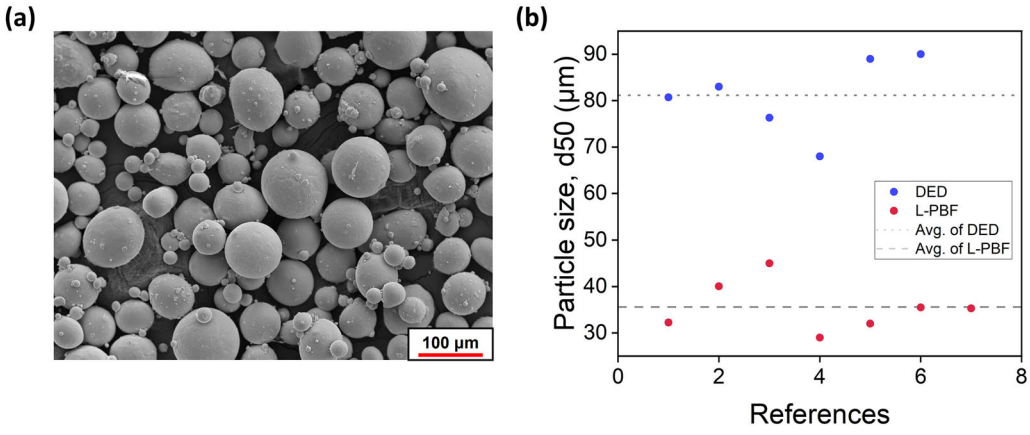

Figure 1. (a) Morphology of Ti–6Al–4V powder used in this work. (b) Particle size distribution (d50) for DED and L-PBF processes in previous literature. The average particle size for DED and L-PBF is 81.2 and 35.6 µm, respectively. The references for DED are in the following order: (Wang et al. 2020; Tandon et al. 2015; Li et al. 2021; Langebeck et al. 2020; Keist, Taminger, and Palmer 2016; Joshi et al. 2021). For the L-PBF, 1-2, 3-4, 5-6, and 7th references are in the following order: (Chen et al. 2022; Meyers et al. 2022; Lu et al. 2022; Englert et al. 2022)

images. The scanned images consisted of 880 × 590 pixels and were visualised in a heatmap according to the relative height in the height set.

2.2 Machine learning

2.2.1 Overview of machine learning

The overview of this study is presented in Figure 3(a). In DED surface morphology prediction via artificial intelligence, an optimised smooth surface design is achieved. To build a dataset specimen, titanium powder was melted and deposited by a laser under various process conditions, thereby generating surfaces with different roughness and quality. CGAN was employed to visualise the expected surface roughness for the given process conditions as shown in Figure 3(b). Given the user input, the expected virtual surface image can be visualised by applying CGAN to the scanned images and process conditions, and the final results are given in 3-dimensional images.

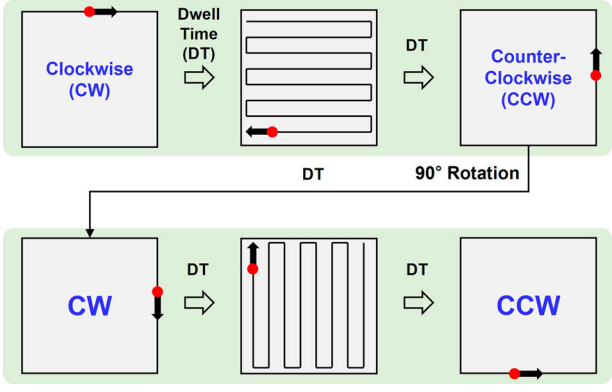

Figure 2. A schematic diagram of the tool path processing unit (Contour – filling – contour). Dwell time is 3.5 s and tool pattern rotation is 90° in a clockwise direction.

2.2.2 Image preprocessing and data augmentation

The dataset was configured by scanning 80 specimens which were split into 9:1 (training set: test set) for CGAN. For the training model using CGAN, as shown in Figure 4, a total of 432 images were augmented by vertical and horizontal flipping and rotation to prevent overfitting during training and increase data diversity (Perez and Wang 2017). In addition, these images were normalised by adjusting the RGB value of the images in the region to between 0 and 1.

The labels for the dataset were constructed by listing the process conditions corresponding to each image, which were normalised to values between 0.1 and 0.9 for each variable. Normalised labels in three process conditions (laser power, powder feed rate, and scan speed) were used as continuous regression forms to train the model. In the case of the generation of the expected surface images from process conditions, the image dataset was resized to 224 × 224 pixels to train the CGAN.

Table 2. Process parameters.

Process parameters (Unit)	Values
Laser power (W)	160, 180, 200, 220
Powder feed rate (g/min)	0.4, 0.5, 0.6, 0.7
Scan speed (mm/min)	850, 890, 925, 960,1000
Dwell time (s)	3.5
Hatch space (mm)	0.3
Layer thickness (mm)	0.15
Laser beam diameter (µm)	400
Laser wavelength (nm)	1090
Shielding gas flow rate (L/min)	8

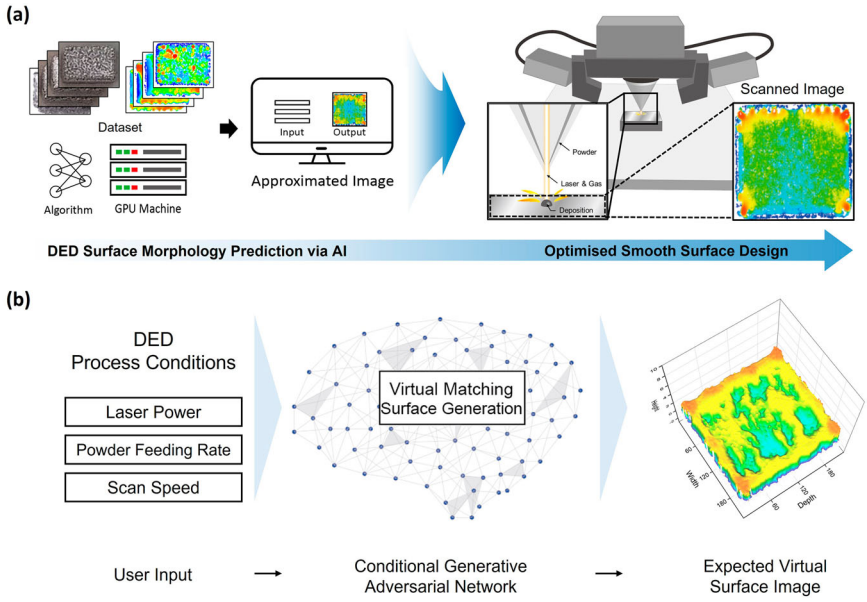

Figure 3. Overview of (a) surface morphology prediction via AI and (b) the surface roughness prediction. A visualisation of the expected virtual surface image suitable for the user input is generated by CGAN.

2.2.3 CGAN architectures for generating the expected surface images

A GAN was used to learn the features of existing image sets to produce an image and output similar to the expected results (Goodfellow et al. 2014). GAN consists of a generator (G) and discriminator (D), such that *G* strives to deceive *D* by generating virtual images, whereas *D* strives to distinguish the real image from the synthetic images generated by *G*. Subsequently, CGAN was developed to add a label to GAN. GAN can generate more real-like samples, which are closer to the ground truth, compared with other generative models even when an explicit data distribution is absent (Alqahtani, Kavakli-Thorne, and Kumar 2021). In addition, GAN does not rely on the Markov chain method which incurs a high computational cost (Gonog and Zhou 2019). Based on these advantages, GAN has been used in various fields for image generation such as medicine (Zhan et al. 2021) and topology optimisation (Shen and Chen 2019). We also implemented this model to visualise the expected surface image.

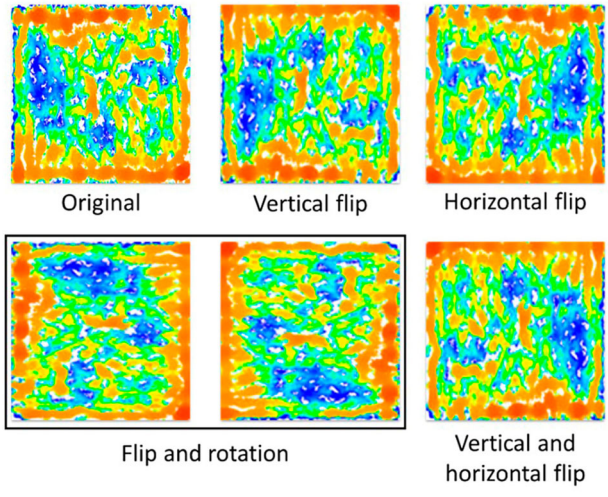

Figure 4. Example of data augmentation for the training set.

CGAN was used to generate virtual images by learning real scanned images, where 2D images of the surface of the DED output were used as the real data. As shown in Figure 5, CGAN consists of two steps, the training and testing steps. In the training step (Figure 5(a)), the three normalised process variables are expressed as a continuous form to generate a label list, which is convolved with random noise and input into *G*. Then *D* identifies real or fake pairs of the generated images based on the real image and label. In the testing step (Figure 5(b)), a predicted surface image can be obtained, similar to the ground truth by entering any three process variables into the trained *G*. The objective function of CGAN is described in Section S1.

A CGAN model was trained on an Ubuntu 18.04 server equipping the AMD Ryzen Threadripper 3990X central processing unit (CPU) and NVIDIA RTX 3090 graphics processing unit (GPU). The processing time for each epoch was approximately 450 milliseconds. For the synthetic images, 128-dimensional uniformly distributed random data were generated, which were then concatenated with 3-dimensional conditions and projected onto

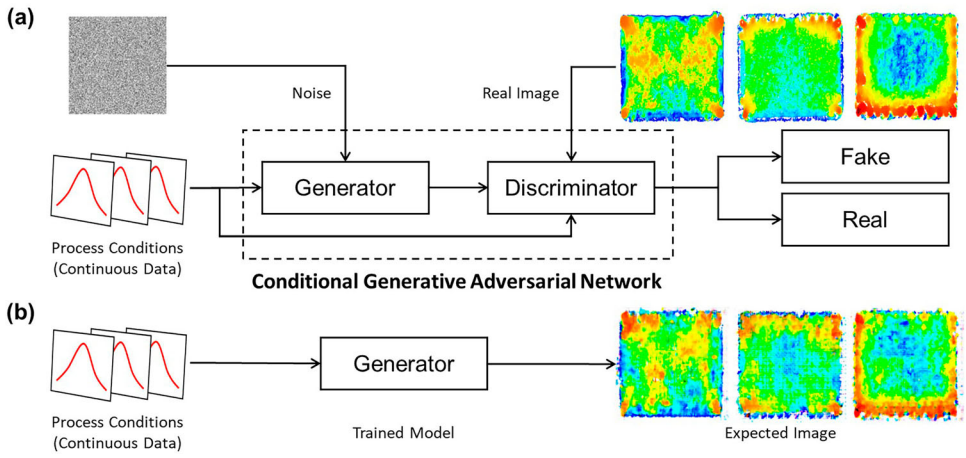

Figure 5. Schematic of how surface roughness is suggested: (a) Training step and (b) testing step. Normalised process conditions are used to train CGAN in the continuous regression form.

G. Then, the output was reshaped and upsampled through four deconvolution processes to produce the 224×224 pixels of an image. The generated image was superimposed onto a real image and its process conditions, which were then downsampled by *D*, through four convolution processes, to enable the classification of the generated image as real or fake. A leaky ReLU (Xu et al. 2015) was used with an alpha of 0.2 as the activation function and the Adam optimiser was used with the default settings for the exponential decay rates. The layers of the model show symmetrical structures of *D* and *G*, as suggested by the original study and some of the other studies (Radford, Metz, and Chintala 2016; Perarnau et al. 2016), which raises the possibility of falling easily into mode collapse (Saxena and Cao 2020; Creswell et al. 2018). To overcome this limitation, hyperparameters were selected by trial and error based on published works, to adjust the learning rate (Luo, Huang, and Li 2021; Al-Shargabi et al. 2021) or the number of hidden layers and filter size (Woldesellasse and Tesfamariam 2022; Heyrani Nobari, Chen, and Ahmed 2021). The details of the hyperparameter selection are discussed in Section 3.2.

The epoch was set to 1000 and Fréchet inception distance (FID) [49], which measures the similarity between real images and generated images, was used to evaluate the generated images. As described in Section S2, since the FID score represents the distance between feature vectors of real and generated images, the lower score means generated image is similar to the real image.

2.2.4 Specimen analysis

An in-depth surface analysis was conducted to investigate the discrepancy between the arbitrary trial case (T specimen) and AI recommended case (R specimen) with the CGAN prediction. T specimen shows arbitrary bad condition which has such characteristic microstructural behaviour as comparative criteria to analyse AI suggested R specimen. Among the examples visualised using CGAN, the process condition for images with uniform surface roughness was selected to manufacture the CGAN recommended case. To analyse the microstructure according to the difference in the surface roughness, an electron backscatter diffraction (EBSD) analysis was performed for each specimen. Moreover, all the sizes of columnar grains were measured in a statistical method by using an image analyser.

To reveal the cause of the anisotropy of the DED process, the cross-sectional structure was analysed using orientation distribution functions (ODFs). For an accurate analysis of typical textures, constant $\Phi_2 = 0$ and 30° ODF maps were used (Fan et al. 2020). The Taylor Francis group (Olaf and Valerie 2009) suggested a standard ODF map of the texture direction and an equation with the Miller index. In addition, the inverse pole figure (IPF) map was used to show the angle of the cropped primary columnar grains, and the primary columnar grains with high GOS values (above 1.5) were cropped from the IPF map.

3. Results & discussion

3.1 Dataset analysis

The scanned images were converted into the HSV (hue, duration, and value) colour space to obtain numerical surface roughness values. The hue, which has the same domain as the colourmap of the scanner, was quantified into surface roughness values. As shown in Figures 6(a)–(c), the average value of the surface roughness ($R_{a,\,avg}$) varies depending on the values of the three process

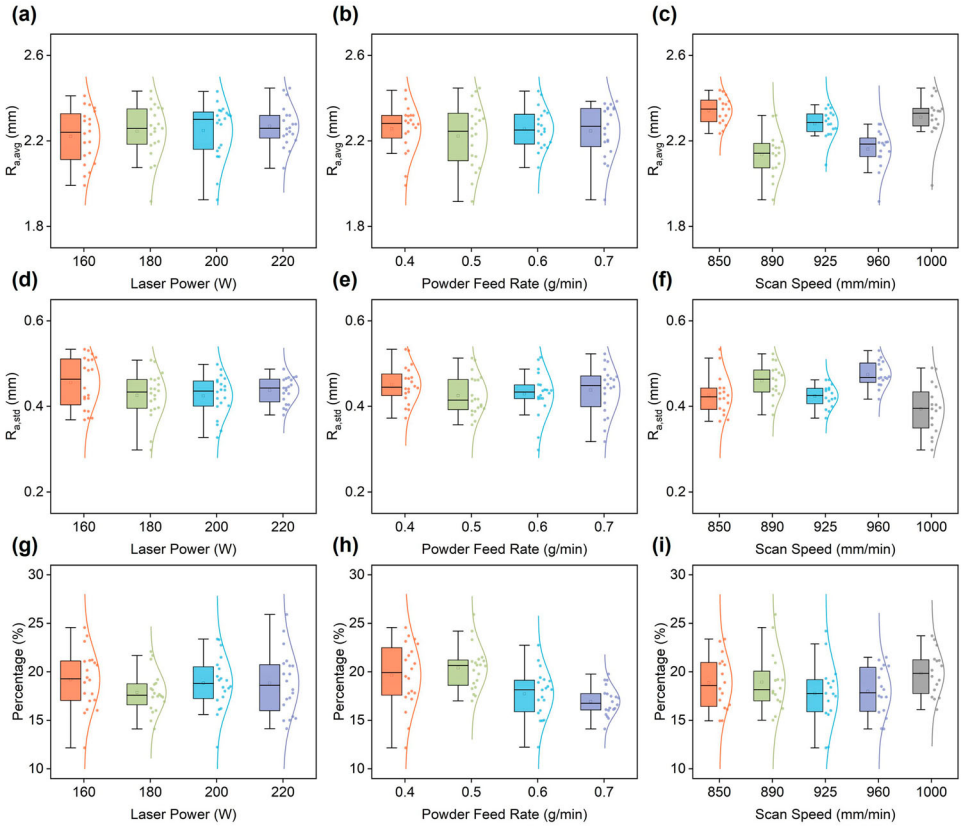

Figure 6. Data used for model learning affected the surface roughness according to the following process conditions: (a)–(c) average of the surface roughness, (d)–(f) standard deviation of surface roughness, and (g)–(i) ratio of blanks, which is outside the measurement range (−0.5–3.0 mm) of the scanned area. The data corresponding to each condition on the x-axis are expressed as dots, and its distribution is represented as a curve. Each box contains data of percentiles between the 25th (Q1) and 75th (Q3). The horizontal central line and square in the box indicate the median and mean. The lower and upper whiskers indicate Q1 − 1.5 × IQR and Q3 + 1.5 × IQR, respectively, where IQR states an interquartile range.

conditions. The $R_{a,avg}$ values were 2.22, 2.24, 2.25, and 2.27 mm according to the laser power, which is not significantly different, but the distribution of the data tends to be dense at 220 W. Some of the samples corresponding to laser power are shown in Figure 7(a). The $R_{a,avg}$ values for the powder feed rate were 2.25, 2.22, 2.26, and 2.24 mm, which are also not significantly different. Unlike other variables, the $R_{a,avg}$ values for the

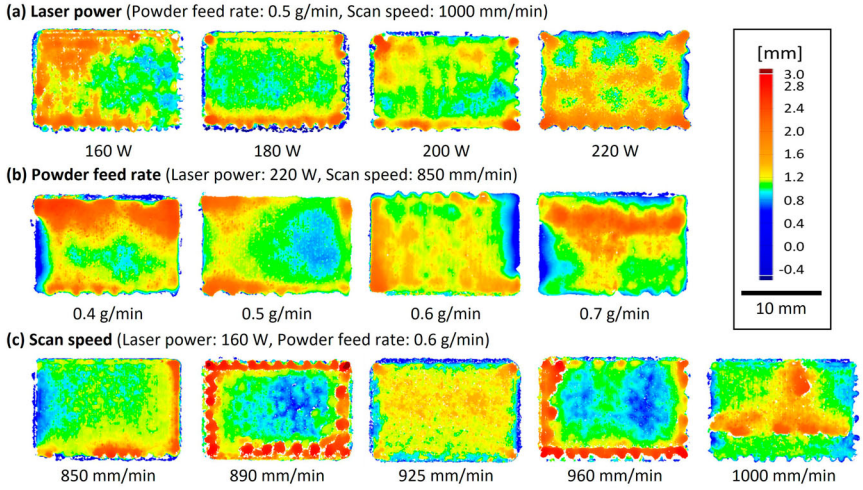

Figure 7. Variation of specimen surface in images as a function of (a) laser power, (b) powder feed rate, and (c) scan speed. Colormap indicates the degree of surface roughness.

scan speed were 2.34, 2.13, 2.28, 2.16 and 2.31 mm, which on average display superior $R_{a,avg}$ values at 890 mm/min. The samples corresponding to powder feed rate and scan speed are shown in Figures 7(b,c). Other than in the parts excluded or not calculated, no clear tendency was observed in the surface roughness in relation to the process conditions.

Figures 6(d–f) indicate the standard deviation values of the surface roughness ($R_{a,std}$). The values of $R_{a,std}$ as a function of the laser powers of 160, 180, 200, and 220 W were 0.45, 0.42, 0.42, and 0.43 mm, respectively displaying low standard deviation values, in general. The values of $R_{a,std}$ according to the powder feed rate of 0.4, 0.5, 0.6, and 0.7 g/min were 0.45, 0.42, 0.43, and 0.44 mm, respectively, showing the lowest standard deviation values at 0.5 g/min. The values of $R_{a,std}$ according to the scan speed 850, 890, 925, 960, and 1000 mm/min were 0.43, 0.46, 0.42, 0.47 and 0.39 mm, respectively. The standard deviation value was the highest when the scan speed was 960 mm/min, indicating that the surface roughness is uniform and close to the target height except for the boundary, compared to other process conditions.

The blank space of scanned images was excluded in the calculation of the average and standard deviation of the surface roughness because they are outside the measurement range of −0.5 mm to 3.0 mm. Consequently, the ratio of blank space was calculated separately as shown in Figure 6(g–i). The blank ratios according to the laser power were 19.2%, 17.9%, 18.9%, and 18.8%, respectively and the lowest value was observed when the laser power was 180 W. In particular, the percentage of the blank under the powder feed rates was 19.7%, 20.4%, 17.7%, and 16.9%, respectively, which tended to significantly decrease as the powder feed rate increased. The blank ratios according to the scan speed were 18.9%, 18.9%, 17.8%, 18%, and 19.8%, respectively similar to the laser power, with the lowest values in the middle of the range.

As shown in Figure 6, no clear tendency was observed experimentally. It means that 80 experimental approaches are not enough to predict the clear effect of each parameter with the given material. Due to this limitation, it is also hard to optimise the process parameters experimentally. Although the surface roughness showed some correlation, there were three process conditions that affected the manufacturing process, making it difficult to determine the effect of each process condition on the surface roughness. Moreover, a large deviation was observed even among data in the same class. Consequently, AI was applied to solve the limitation of AM, predicting the surface morphology from the process conditions. The results are presented in the following sections.

3.2 Model optimisation

To obtain the best results, some variations were studied as shown in Figures 8(a–d). The first case of Figure 8(e) is the base structure, and variations on the first case are numbered from 2 to 5. The corresponding FID score for each case is summarised in Figures 8(e,f). Because the discriminator loss converges to zero rapidly, to balance the performance of both the generator and discriminator, the hyperparameters of the generator were modified. In cases 1 and 2, where the generator and discriminator were structurally identical as shown in Figures 8(a,b), the FID scores were 288.2 and 284.5, respectively. A reduction in the number of convolutional layer filters in the discriminator (Case 3) resulted in an FID score of 191.6, which is a decrease of 33.52% compared to that of the base structure (Case 1). In case 4, which has a reduced number of hidden layers in the discriminator, FID decreased by 8.3% to 264.4. However, case 5 is structurally identical to case 1, but when the learning rates of the generator and discriminator were set to 0.0002 and 0.0001, respectively, the FID score decreased by 39.4% to 174.8, which indicates a more balanced update of both the generator and discriminator. The details of the FID scores and losses for the entire learning process is shown in Figure 9. Although the model was optimised properly for a given data, model optimisation and training process may be required if the updated data or other types of data deviate from the existing data distribution.

The loss of the generator and discriminator is displayed in Figure 9(a). The generator loss of cases 1 and 2, which are structurally symmetrical, converged to 0 after 500 epochs whereas the discriminator loss diverged as model learning progressed. The generator loss of case 3 converged to 0 from 300 epochs, but both generator and discriminator losses oscillated after 700 epochs. The generator loss of case 4 converged to 0.8 from 300 epochs whereas the discriminator loss converged to 0. For case 5, generator and discriminator losses oscillated, and then converged to 0.2 and 2, respectively, after 700 epochs (Figure S1). The FID scores of these two cases were worse than other cases, as shown in Figure 9(b). However, in the case of the asymmetric model, the generator loss did not converge to 0, and the FID score was also superior to the symmetric case. As the FID of case 5 is minimum, the selected optimal hyperparameters are the same as case 5: the number of filters in the hidden layer of generator and discriminator is (512, 256, 128, 64) and (64, 128, 256, 512), respectively, and the learning rate of generator and discriminator is 0.0002 and 0.0001, respectively. It is observed that in Figure 9(b), our optimised model structure displays an improved FID score for the test set.

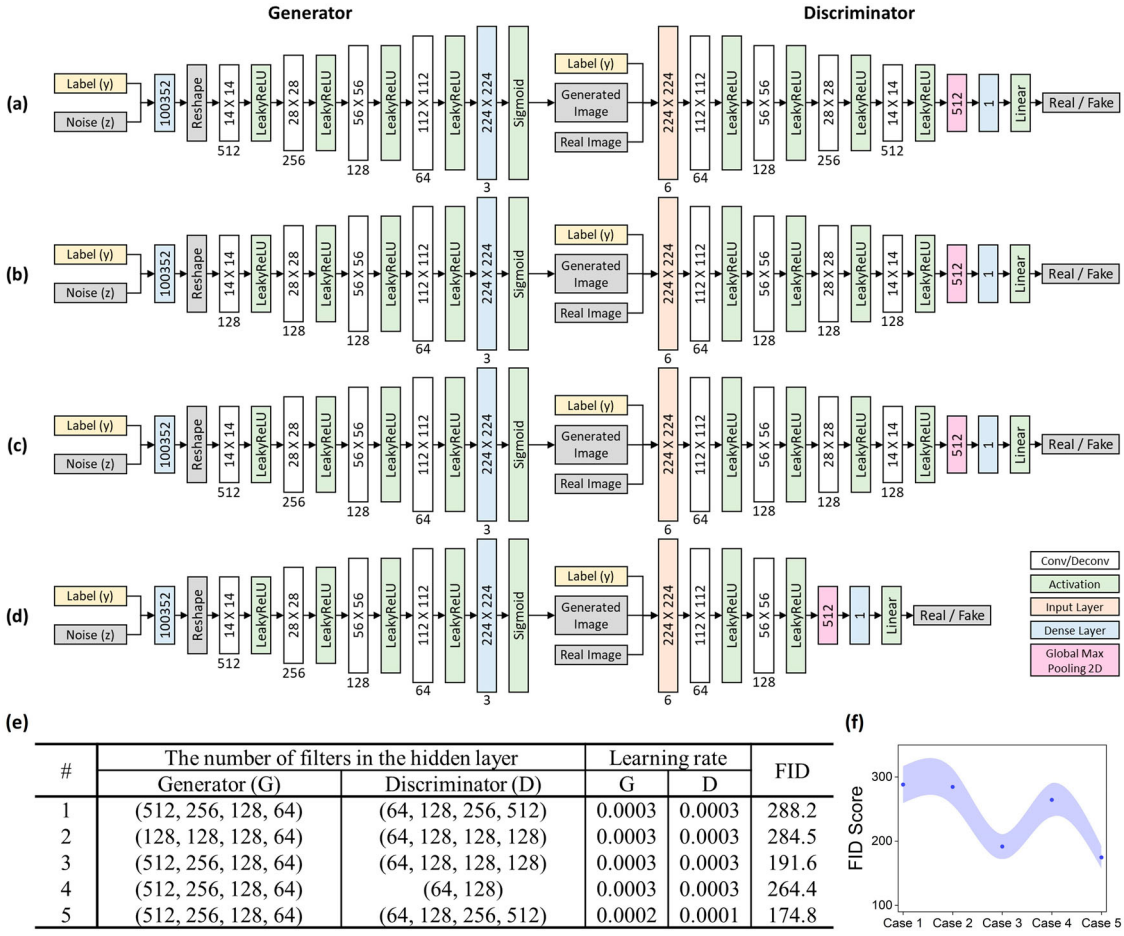

(e)

#	The number of filters in the hidden layer		Learning rate		FID
	Generator (G)	Discriminator (D)	G	D	
1	(512, 256, 128, 64)	(64, 128, 256, 512)	0.0003	0.0003	288.2
2	(128, 128, 128, 64)	(64, 128, 128, 128)	0.0003	0.0003	284.5
3	(512, 256, 128, 64)	(64, 128, 128, 128)	0.0003	0.0003	191.6
4	(512, 256, 128, 64)	(64, 128)	0.0003	0.0003	264.4
5	(512, 256, 128, 64)	(64, 128, 256, 512)	0.0002	0.0001	174.8

(f)

Figure 8. Various CGAN architectures for model optimisation: (a) case 1 and 5, (b) case 2, (c) case 3, and (d) case 4. In terms of filter size of hidden layers, (a, b) show symmetric and balanced structures, while (c, d) show asymmetric structures. Case 1 and 5 have the same structures but different learning rates. For each case, the (e) selected hyperparameters and (f) FID score with shaded areas, indicate an error of 5%.

3.3 Prediction result

The images of the surface roughness created with this CGAN are plotted in 3-dimensional profiles (Figures 10 and 11) and the surface roughness prediction was performed using the CGAN with several process conditions which are given in Table 3. The overall surface roughness and the distribution of the generated image matched those of the scanned image for both smooth surfaces (Figure 10) and rough surfaces (Figure 11). The smooth surfaces cover a large portion of the uniform surface roughness in the scanned image, with the surfaces generated by CGAN, displayed in the blue and green areas, appearing evenly in the specimen. However, the generated rough surface has white spaces all over the surface, which are areas outside the measurement, and surface roughness is generally not uniform, similar to the actual image. The process conditions through AI guidance were selected as shown in Table 3, and the prediction and actual formulation results are shown in Figure 12. As shown in Table 3, the prediction of conditions 2 and 3 shows different surface roughness despite slight differences in process conditions. As shown in the generated image (Figure 10(b)), the expected surface roughness of condition 2 has a uniform and continuous surface at the centre part, and the surface roughness increases at the edge of the specimen. However, the expected surface roughness of condition 3 (Figure 11(a)) is discontinuous overall, similar to the actual specimen manufactured, and the surface roughness is high not only at the specimen edge but also at the centre part. Various virtual surface morphology prediction results are summarised in Tables S2 and S3.

3.4 Specimen analysis

As shown in Figure 13, a 3D scanning image and scanning electron microscope (SEM) analysis were employed

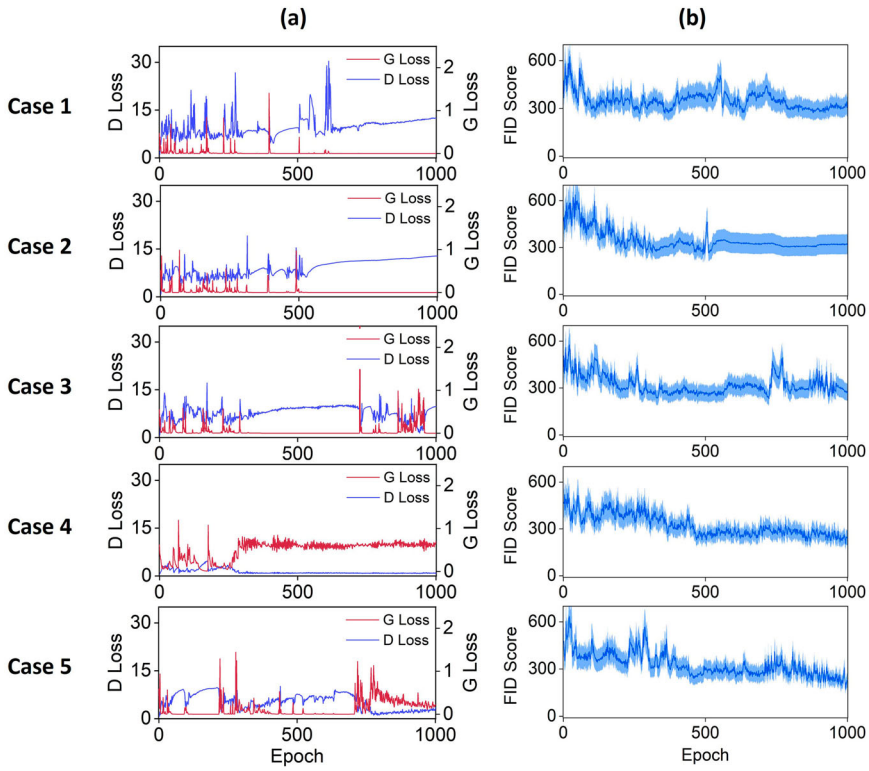

Figure 9. CGAN model training result: (a) Discriminator loss (D Loss) and generator loss (G loss) and (b) FID score for 5 cases.

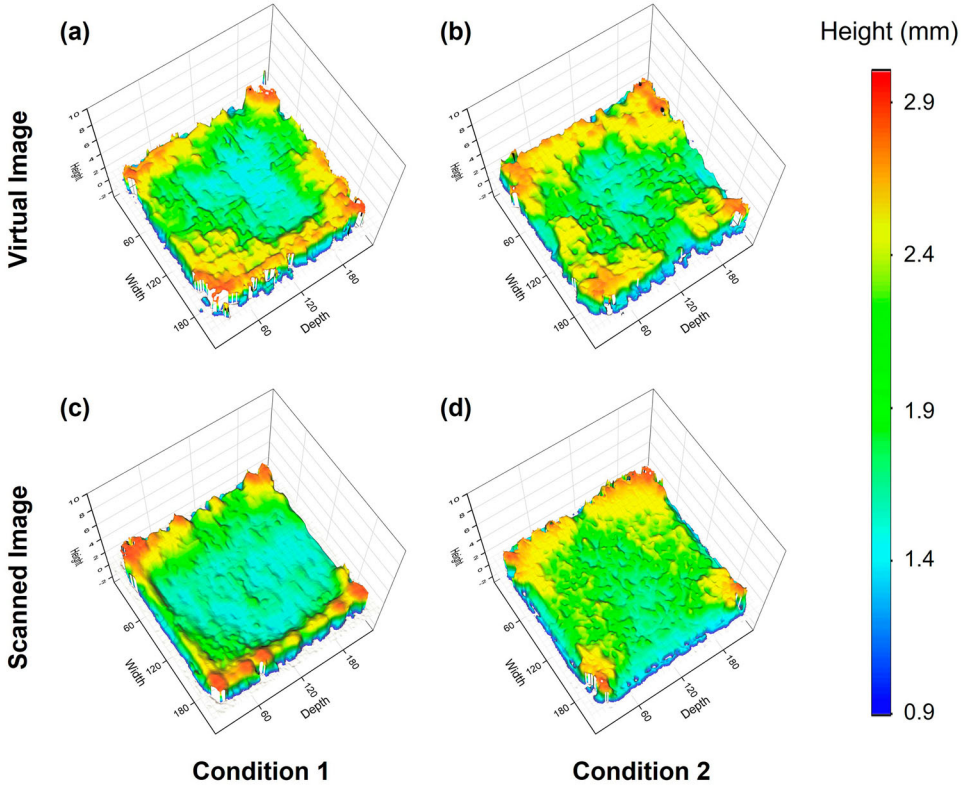

Figure 10. (a, b) Generated virtual images and (c, d) scanned images of smooth surfaces that were manufactured from the given process conditions used in the CGAN. The colourmap indicates the difference between target height and printed height.

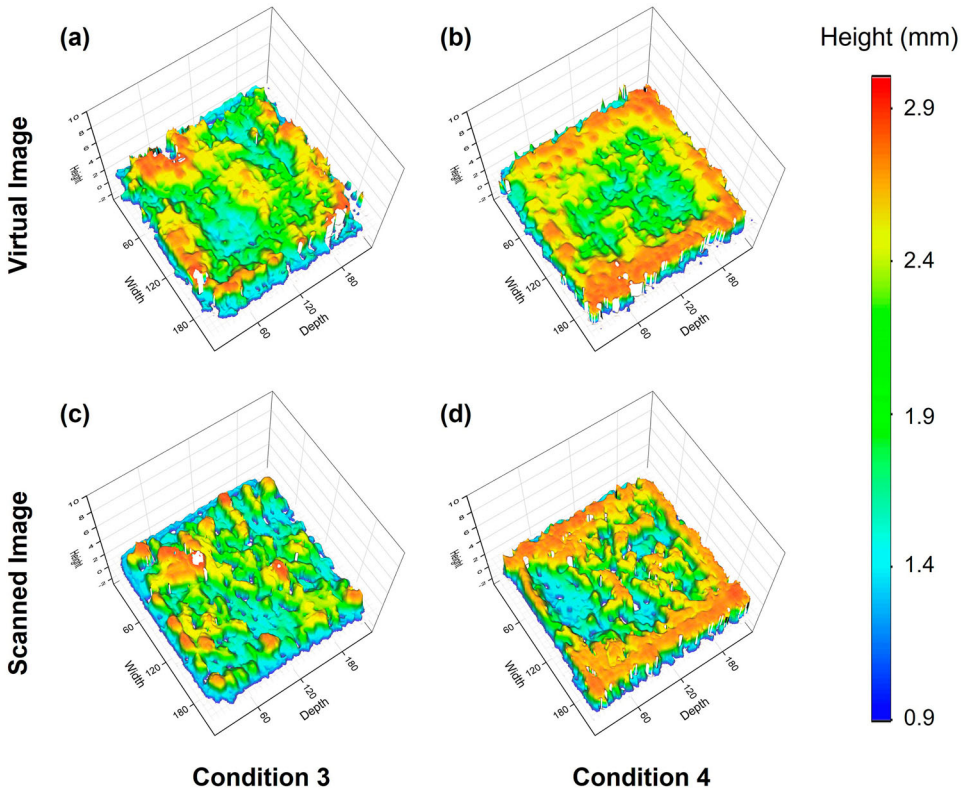

Figure 11. (a, b) Generated virtual images and (c, d) scanned images of rough surfaces that were manufactured from the given process conditions used in the CGAN.

Table 3. Used process conditions for samples.

	Figure 10		Figure 11		Figure 12
Parameter	Condition 1	Condition 2	Condition 3	Condition 4	AI Guidance
Laser power (W)	180	160	160	160	193
Powder feed rate (g/min)	0.5	0.5	0.4	0.4	0.5
Scan speed (mm/min)	960	925	1000	850	919

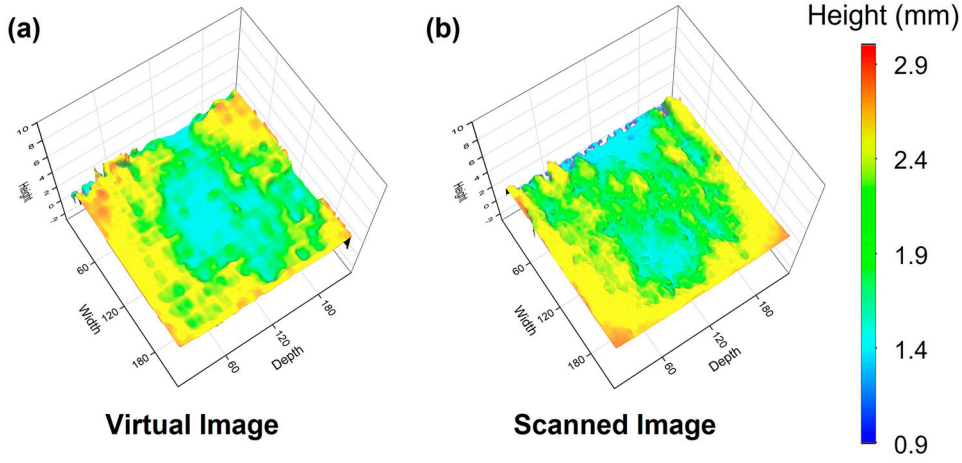

Figure 12. The virtual surface of AI-guided process condition and experimental fabricated scan surface image

for the surface analysis of the T and R specimens. The comparison of the 3D scanned results in Figures 13(a,c) shows that the R specimen is more uniformly distributed than the T specimen. In the T specimen with a large surface roughness, the areas with high and low heights are referred to as the T-1 and T-2 regions, respectively. In the R specimen with a low surface roughness, EBSD analysis was performed in area R-1, as shown in Figure 14.

The EBSD specimens were extracted from the T-1, T-2, and R-1 regions, as shown in Figure 14, and their image quality (IQ) maps are shown in Figure S2. Widmanstätten martensite structures were present in both regions reflecting the supercooling during solidification. The cooling rate of the DED process for fabricating Ti–6Al–4V was above 10^4 °C/s, which is sufficient to form acicular microstructures (Qian et al. 2005; Yu et al. 2012). Secondary columnar grains show a low grain orientation spread (GOS) value compared to the primary columnar grains because of the negligible effect of thermal stress. The texture of the T-1 and T-2 regions had a dominant orientation, with the highest plane being $(10\bar{1}0)$ and $(3\bar{1}\bar{2}3)$, whereas no dominant orientation was formed in the R-1 region. Therefore, the T-1 region showed a higher solidification rate than the R-1 region. This reveals that formation of secondary columnar grains was encouraged in the R-1 region due to higher solidification rate compared to T-1 region. In the general method of fabricating Ti–6Al–4V, the liquid phase first transforms to the β phase and then to the primary α′-martensite. However, in the DED process, the β phase at the peak temperatures directly transforms into another type of fine α′ martensite during cooling. The growth rate along the axial direction of α′-martensite is higher than that in the radial direction, which means that α′-martensite is highly anisotropic with a high aspect ratio (Lu et al. 2020; Yadollahi et al. 2017). In Figure 14(h), the acicular α′-laths martensites are composed of high-angle grain boundaries at approximately 60°. The width and length of the average primary columnar grain in the R-1 region were 4.9 and 76.9 μm, respectively, which is in the mid-range between the T-1 (6.2 and 107.5 μm) and T-2 (3.4 and 53.4 μm) regions.

Here, the standard ODF map of $\Phi_2 = 0°$ and 30° is presented in Figure 15(a). In the ODF map of $\Phi_2 = 0°$ and 30°, the arbitrary specimens (T-1 and T-2) have a strong $\{0001\}\langle 10\bar{1}0 \rangle$ prismatic texture (□, ○, Δ, ◇) and a relatively weak basal texture. However, the texture characteristics of the CGAN recommended specimen (R-1) were not strong in the ODF map. In particular, the intensity of the texture was gradually offset from point $(01\bar{1}0)[2\bar{1}\bar{1}\bar{1}]$ at the ODF map of $\Phi_2 = 30°$ (in the order T-1, T-2, and R-1).

The results show the fractional numbers of columnar growth angle (α), for the build direction in Figures 16(b, e,h). The primary columnar grains in the T-1 region were concentrated at 10°–20°, whereas they are within 20°–40° in the build direction in the T-2 region. However, the primary columnar grains in the R-1 region were located at 30° to the build direction. The primary columnar grains in the T-1 and T-2 regions showed a typical texture morphology of the hcp structure, whereas those in the R-1 region had low texture intensity in all planes. The T-1 region had a strong texture in the (0001), $(10\bar{1}0)$, and $(11\bar{2}0)$ planes. The high cooling rate of the T-1 region promoted the growth kinetics in the

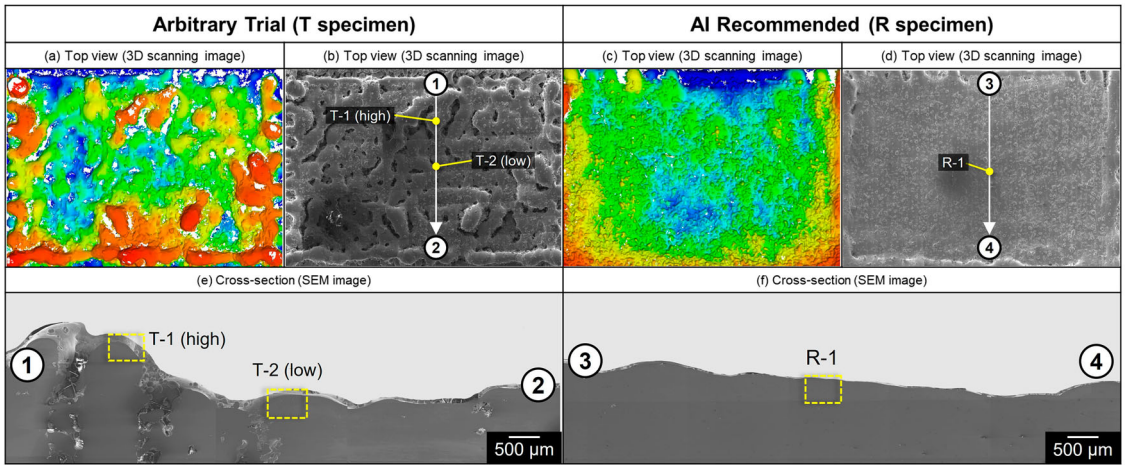

Figure 13. Comparative analysis of the surface roughness between the product with randomly chosen process conditions (T specimen) and the product with thoroughly chosen process conditions following AI recommendation (R specimen). Surface analysis of (a, c) the 3D scan image and (b, d) scanning electron microscope (SEM) image. (e, f) SEM images of the cross-sectional view of each specimen.

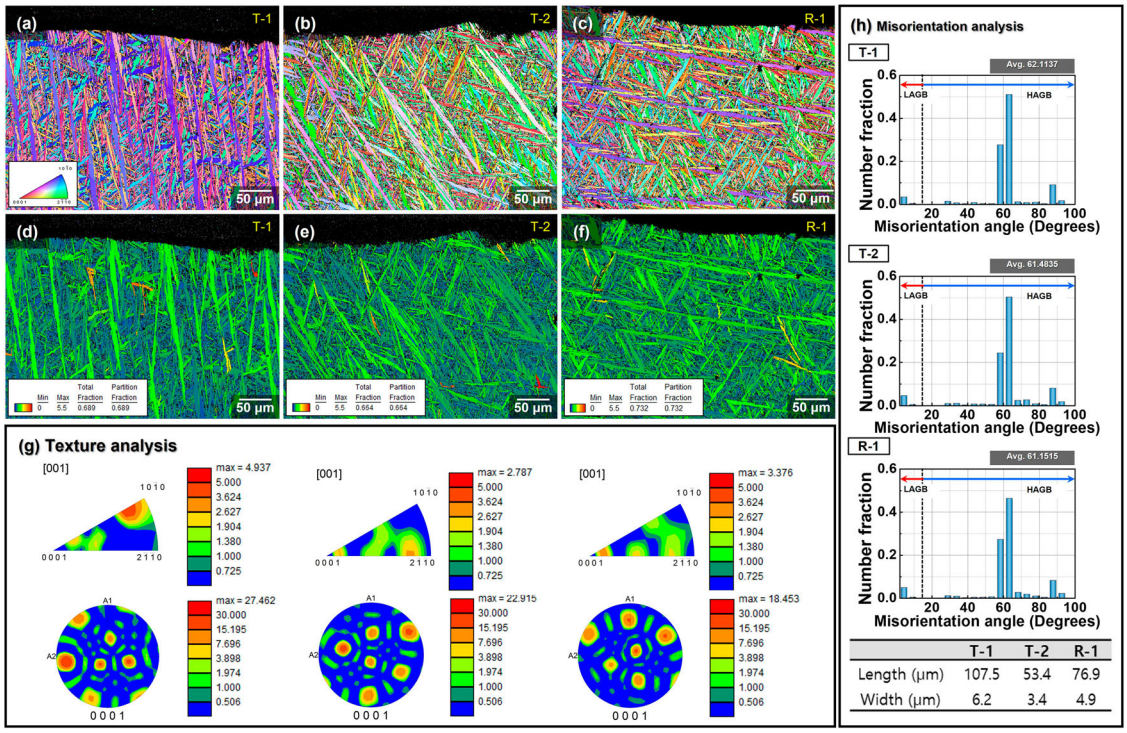

Figure 14. EBSD analysis of arbitrary trial and AI recommended specimen on the cross-sectional view: (a, d) T-1, (b, e) T-2, and (c, f) R-1 regions. Each map shows (a–c) the inverse pole figure (IPF) map and (d–f) grain orientation spread (GOS) map (when the maximum GOS value is 5.5). (g) Texture analysis of the T-1, T-2, and R-1 specimens. The IPF ranged from 0 to 5, and the pole figure (PF) ranged from 0 to 30. (h) Chart of the misorientation fraction and table of the primary columnar grain size. In the PF, the T-1, T-2, and R-1 regions have maximum values of 27.462, 22.915, and 18.453, respectively.

primary grains with high texture. Chandramohan et al. and Sridharan et al. reported that the L-PBF-processed Ti–6Al–4V alloy had a strong [0001] texture along the building direction due to the high cooling rate (Chandramohan 2019; Sridharan et al. 2016). Esmaily et al. also suggested that a strong texture of the basal plane was formed in the L-PBF processed specimens, and the c-axis of the hcp structure was almost parallel to the build direction (Esmaily et al. 2020).

In the T-1 region, the primary columnar grains had the longest length and the smallest angle (α) in the build direction, whereas the length and angle (α) of the T-2 region were relatively lower. This is attributed to the high cooling rate of the T-1 region compared to the T-2 region because of the higher altitude of the former. Despite the different morphologies of the primary columnar grains, both regions showed strong textures, as shown in Figures 16(c,f). In the R-1 region, the length of the primary columnar grains was shorter, and the angle (α) was wider than those in the T-1 and T-2 regions. The weak textures are shown in the (0001), $(10\bar{1}0)$, and $(11\bar{2}0)$ planes. In general, in DED-processed Ti–6Al–4V alloys, anisotropic properties are inevitably obtained by the highly textured columnar grain microstructure formed during solidification. However, in this study, a weakly textured microstructure is proposed without strong anisotropic microstructure, using AI. This method also enables microstructure control of DED-processed Ti–6Al–4V alloys by obtaining surface roughness image data.

There is still a limitation that this study requires initial enough experiments as training data, which is also a bottleneck for most AI used in manufacturing fields. However, once this AI model is developed, it can be used as a powerful tool to immediately confirm the surface morphology for a much diverse uncovered range of process conditions with high accuracy. As the developed AI can generate various levels of surface roughness, the developed AI may be also used in generating hybrid-type surfaces with several different amounts of roughness for various purposes.

4. Conclusion

In this study, the CGAN-assisted surface morphology prediction method is developed for Ti-6Al-4V DED parts by optimisation of neural network structures. The experimental results and predictions illustrate the effectiveness of the developed CGAN model for choosing the optimal process conditions for manufacturing metal parts through AM. The primary conclusions are presented as follows:

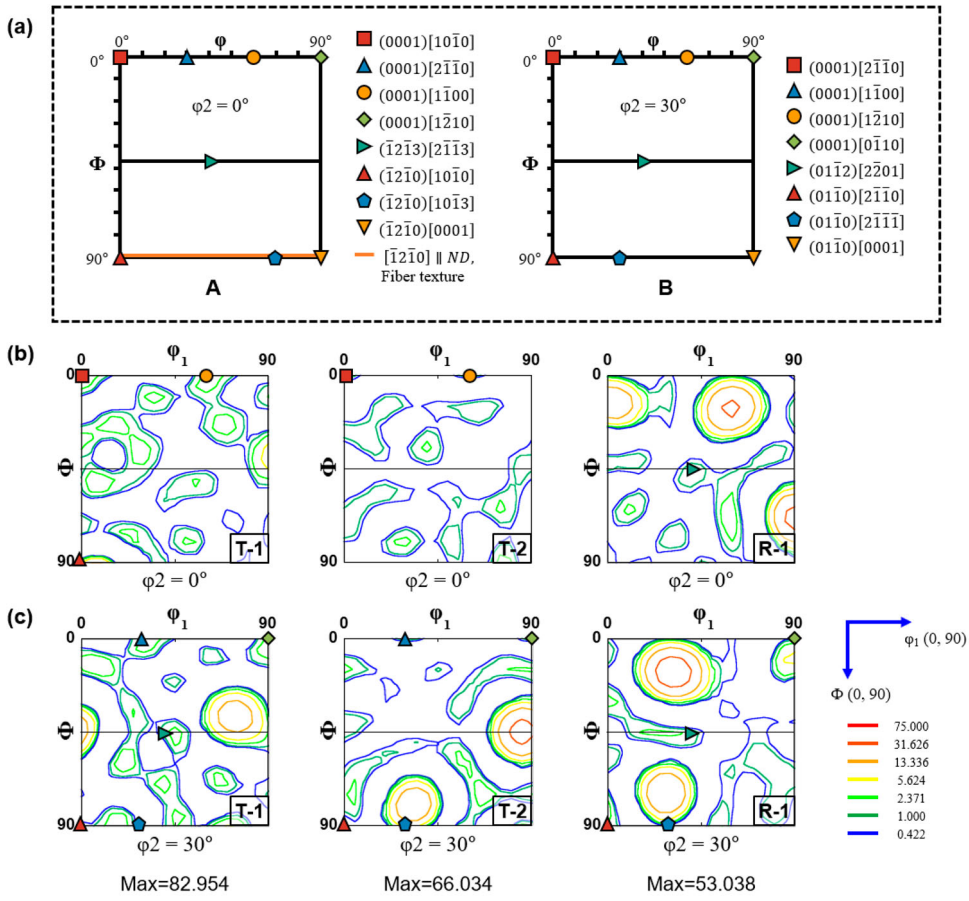

Figure 15. (a) Standard orientation distribution function (ODF) maps of the hexagonal close-packed (HCP): (A) φ2 = 0°, (B) φ2 = 30° (Fan et al. 2020). ODF of the T-1, T-2, and R-1 regions for (b) φ2 = 0° and (c) φ2 = 30°. When the range of the ODF map is from 0 to 75, the maximum values of the T-1, T-2, and R-1 regions are 82.954, 66.034, and 53.038, respectively. The texture intensity is the highest in the T-1 region.

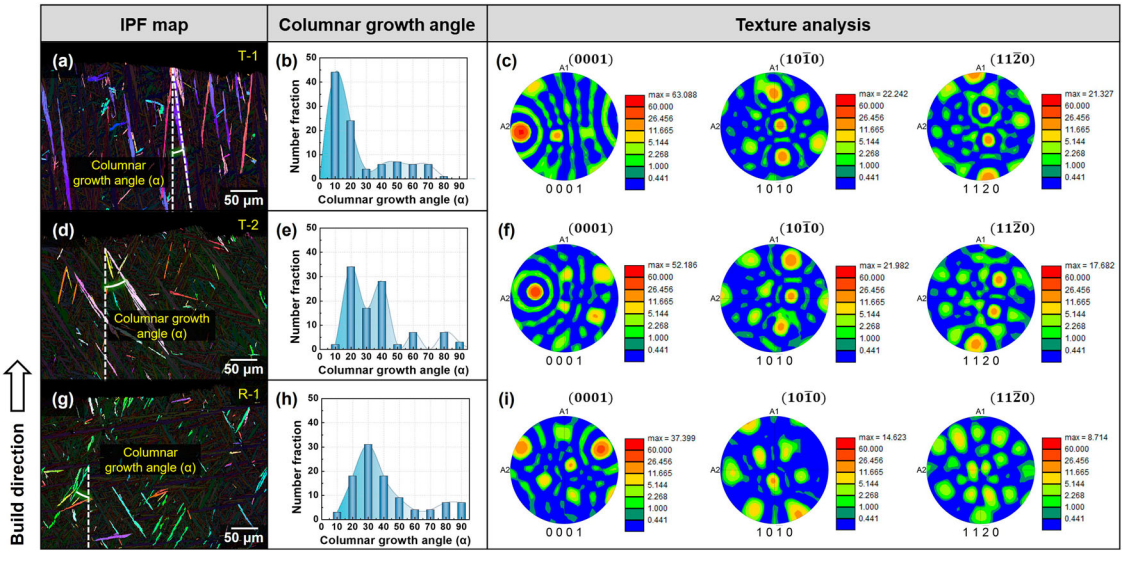

Figure 16. The inverse pole figure (IPF) map of (a) T-1, (d) T-2, and (g) R-1 regions showing the angle of the cropped primary columnar grains. The primary columnar grains have high grain orientation spread (GOS) values between 1.5 and 5.5. (b, e, h) Distribution of angles between the primary columnar grain and build direction. (c, f, i) pole figure (PF) shows the texture analysis of the primary columnar grains in the (0001), (10$\bar{1}$0), and (11$\bar{2}$0) planes. When the PF ranges from 0 to 60, the maximum values of the (c) T-1, (f) T-2, and (i) R-1 regions are 63.088, 52.186, and 37.399 in the (0001) plane, respectively. The texture intensity is the highest in the (0001) plane as compared to those in the (10$\bar{1}$0) and (11$\bar{2}$0) planes.

1. With the help of the developed AI process with a high FID score, the virtual surface morphology images of the Ti-6Al-4V DED part were successfully generated from identical process conditions.
2. The virtual surface of DED parts matches the printed metal surface well in terms of appearance and SEM analysis as well as quantitative study in microstructural analysis near the surface.
3. The CGAN-assisted quick virtual surface generation and its corresponding Ti-6Al-4V DED part had an improved smooth surface with less lack of fusion or surface defects.
4. Diverse range of DED process parameters can be quickly checked for their corresponding surface morphology with high accuracy by the developed AI. The developed methodology using CGAN can also be used for further studies with side surface, edge, or curved surface morphology.

Disclosure statement

No potential conflict of interest was reported by the author(s).

Funding

This work was supported by the Ulsan National Institute of Science and Technology (grant nymber 1.210129.01), the National Research Foundation of Korea (grant number 2021M2D2A1A01050059, 2021R1F1A1046079, and 2020R1A4A3079417), the Korea Institute of Energy Technology Evaluation and Planning (KETEP) grant funded by the Ministry of Science and ICT (20214000000480, Development of R&D engineers for combined cycle power plant technologies).

CRediT authorship contribution statement

Taekyeong Kim: Conceptualisation, Data curation, Investigation, Methodology, Formal analysis, Visualisation, Software, Writing – original draft, Writing – review & editing. **Jung Gi Kim:** Data curation, Investigation, Formal analysis, Software, Writing – original draft. **Sangeun Park:** Investigation, Formal analysis, Visualisation, Writing – original draft. **Hyoung Seop Kim, Namhun Kim, Seung-Kyum Choi:** Formal analysis, Supervision. **Hyunjong Ha:** Data curation, Formal analysis. **Conrad Tucker:** Formal analysis, Writing – original draft, Supervision, Investigation. **Hyokyung Sung, Im Doo Jung:** Conceptualisation, Data curation, Investigation, Methodology, Formal analysis, Visualisation, Supervision, Software, Writing – original draft, Writing – review & editing.

Notes on contributors

Taekyeong Kim is a graduate student at the Ulsan National Institute of Science and Technology. His current research interests include artificial intelligence for manufacturing and digital twin.

Jung Gi Kim is an assistant professor at the Department of Materials Engineering and Convergence Technology, Gyeongsang National University. His current research interest includes additive manufacturing for extreme structural metallic materials.

Sangeun Park is a graduate student at the Gyeongsang National University.

Hyoung Seop Kim is a professor at the Department of Materials Science and Engineering, Pohang University of Science and Technology. His research interest includes finite element modeling of metal additive manufacturing, high entropy alloy, and severe plastic deformation.

Namhun Kim is a professor at the Department of Mechanical Engineering, Ulsan National Institute of Science and Technology (UNIST) and director of the Center for 3D Printing Advanced Additive Manufacturing. His research interest includes Design for Additive Manufacturing and Manufacturing Process Engineering.

Hyunjong Ha is a researcher at the Korea Institute of Materials Science.

Seong-Kyum Choi is an associate professor at the Department of Mechanical Engineering, Georgia Institute of Technology. His research interests include structural reliability, probabilistic mechanics, artificial intelligence approaches to the design of structural systems, multidisciplinary design optimization, and additive manufacturing.

Conrad Tucker is a professor at the Department of Mechanical Engineering, Carnegie Mellon University.

Hyokyung Sung is an associate professor at the Department of Materials Science & Engineering, Kookmin University. His research interests include microstructural characterization and mechanical testing for additively manufactured materials.

Im Doo Jung is an assistant professor at the Department of Mechanical Engineering, Ulsan National Institute of Science and Technology (UNIST). His research interest includes artificial intelligence for the digitalization of manufacturing and metal/electrical material development.

ORCID

Taekyeong Kim http://orcid.org/0000-0002-4016-4742
Hyokyung Sung http://orcid.org/0000-0002-1734-1683
Im Doo Jung http://orcid.org/0000-0003-0883-1848

References

Akbari, Mohammad, Seyfolah Saedodin, Afshin Panjehpour, Mohsen Hassani, Masoud Afrand, and Mohammad Javad Torkamany. 2016. "Numerical Simulation and Designing Artificial Neural Network for Estimating Melt Pool Geometry and Temperature Distribution in Laser Welding

of Ti-6Al-4V Alloy." *Optik* 127 (2): 11161–11172. Elsevier GmbH. doi:10.1016/j.ijleo.2016.09.042.

Al-Shargabi, Amal A, Jowharah F. Alshobaili, Abdulatif Alabdulatif, and Naseem Alrobah. 2021. "Covid-Cgan: Efficient Deep Learning Approach for Covid-19 Detection Based on Cxr Images Using Conditional Gans." *Applied Sciences (Switzerland)* 11: 16. doi:10.3390/app11167174.

Alqahtani, Hamed, Manolya Kavakli-Thorne, and Gulshan Kumar. 2021. "Applications of Generative Adversarial Networks (GANs): An Updated Review." *Archives of Computational Methods in Engineering* 28 (2): 525–552. Springer Netherlands. doi:10.1007/s11831-019-09388-y.

Amato, Filippo, Alberto López, Eladia María Peña-Méndez, Petr Vaňhara, Aleš Hampl, and Josef Havel. 2013. "Artificial Neural Networks in Medical Diagnosis." *Journal of Applied Biomedicine* 11 (2): 47–58. doi:10.2478/v10136-012-0031-x.

Ang, Yao Ting, Swee Leong Sing, Joel Choon, and Wee Lim. 2022. "Process Study for Directed Energy Deposition of 316L Stainless Steel with TiB 2 Metal Matrix Composites. no. July. doi:10.18063/msam.v1i2.13.

Barroqueiro, B., A. Andrade-Campos, R. A. F. Valente, and V. Neto. 2019. "Metal Additive Manufacturing Cycle in Aerospace Industry: A Comprehensive Review." *Journal of Manufacturing and Materials Processing* 3 (3): 1–21. doi:10.3390/jmmp3030052.

Bennett, Jennifer, Daniel Garcia, Marie Kendrick, Travis Hartman, Gregory Hyatt, Kornel Ehmann, Fengqi You, and Jian Cao. 2019. ""Repairing Automotive Dies with Directed Energy Deposition: Industrial Application and Life Cycle Analysis." *Journal of Manufacturing Science and Engineering, Transactions of the ASME* 141 (2): 1–9. doi:10.1115/1.4042078.

Blakey-Milner, Byron, Paul Gradl, Glen Snedden, Michael Brooks, Jean Pitot, Elena Lopez, Martin Leary, Filippo Berto, and Anton du Plessis. 2021. "Metal Additive Manufacturing in Aerospace: A Review." *Materials & Design* 209: 110008. The Author(s). doi:10.1016/j.matdes.2021.110008.

Caiazzo, Fabrizia, and Alessandra Caggiano. 2018. "Laser Direct Metal Deposition of 2024 Al Alloy: Trace Geometry Prediction via Machine Learning." *Materials* 11 (3). doi:10.3390/ma11030444.

Chandramohan, P. 2019. "Laser Additive Manufactured Ti-6Al-4V Alloy: Texture Analysis." *Materials Chemistry and Physics* 226 (October 2018): 272–278. Elsevier. doi:10.1016/j.matchemphys.2019.01.035.

Chen, Jie, Yongqiang Yang, Yuchao Bai, Di Wang, Cuiling Zhao, and Jerry Ying Hsi Fuh. 2022. "Single and Multiple Track Formation Mechanism of Laser Powder Bed Fusion 316L/CuSn10 Multi-Material." *Materials Characterization* 183 (June 2021): 111654. Elsevier Inc. doi:10.1016/j.matchar.2021.111654.

Creswell, Antonia, Tom White, Vincent Dumoulin, Kai Arulkumaran, Biswa Sengupta, and Anil A. Bharath. 2018. "Generative Adversarial Networks: An Overview." *IEEE Signal Processing Magazine* 35 (1): 53–65. doi:10.1109/MSP.2017.2765202.

Denlinger, Erik R., Jarred C. Heigel, Pan Michaleris, and T. A. Palmer. 2015. "Effect of Inter-Layer Dwell Time on Distortion and Residual Stress in Additive Manufacturing of Titanium and Nickel Alloys." *Journal of Materials Processing Technology* 215: 123–131. Elsevier B.V. doi:10.1016/j.jmatprotec.2014.07.030.

Dharmawan, Audelia Gumarus, and Gim Song Soh. 2022. "A Cylindrical Path Planning Approach for Additive Manufacturing of Revolved Components." *Materials Science in Additive Manufacturing* 1 (1): 3. doi:10.18063/msam.v1i1.3.

Doñate-Buendia, C., P. Kürnsteiner, F. Stern, M. B. Wilms, R. Streubel, I. M. Kusoglu, J. Tenkamp, et al. 2021. "Microstructure Formation and Mechanical Properties of ODS Steels Built by Laser Additive Manufacturing of Nanoparticle Coated Iron-Chromium Powders." *Acta Materialia* 206, doi:10.1016/j.actamat.2020.116566.

Dutta, Bhaskar. 2020. "Directed Energy Deposition (DED) Technology." *Encyclopedia of Materials: Metals and Alloys*, 66–84. doi:10.1016/b978-0-12-819726-4.00035-1.

Englert, Lukas, Anselm Heuer, Mathias Keanu Engelskirchen, Felix Frölich, Stefan Dietrich, Wilfried V. Liebig, Luise Kärger, and Volker Schulze. 2022. "Hybrid Material Additive Manufacturing: Interlocking Interfaces for Fused Filament Fabrication on Laser Powder Bed Fusion Substrates." *Virtual and Physical Prototyping* 17 (3): 508–527. doi:10.1080/17452759.2022.2048228.

Esmaily, M., Z. Zeng, A. N. Mortazavi, A. Gullino, S. Choudhary, T. Derra, and F. Benn. 2020. "A Detailed Microstructural and Corrosion Analysis of Magnesium Alloy WE43 Manufactured by Selective Laser Melting." *Additive Manufacturing* 35 (May): 101321. Elsevier. doi:10.1016/j.addma.2020.101321.

Fan, Jiangkun, Hao Huang, Xiangyi Xue, Wenyuan Zhang, and Yang Wang. 2020. "Hot Rolled Ti6321 Alloy Sheets With Different Initial Microstructures : Microstructure, Mechanical Properties, and Anisotropy Characteristics." *Frontiers in Materials* 7 (May): 1–11. doi:10.3389/fmats.2020.00110.

Farzaneh, Aidin, Mahyar Khorasani, Ehsan Farabi, Ian Gibson, Martin Leary, Amirhossein Ghasemi, and Bernard Rolfe. 2022. "Sandwich Structure Printing of Ti-Ni-Ti by Directed Energy Deposition." *Virtual and Physical Prototyping*. doi:10.1080/17452759.2022.2096647.

Gharbi, Myriam, Patrice Peyre, Cyril Gorny, Muriel Carin, Simon Morville, Philippe Le Masson, Denis Carron, and Rémy Fabbro. 2013. "Influence of Various Process Conditions on Surface Finishes Induced by the Direct Metal Deposition Laser Technique on a Ti-6Al-4V Alloy." *Journal of Materials Processing Technology* 213 (5) 791–800. Elsevier B.V. doi:10.1016/j.jmatprotec.2012.11.015.

Gonog, Liang, and Yimin Zhou. 2019. "A Review: Generative Adversarial Networks." *Proceedings of the 14th IEEE Conference on Industrial Electronics and Applications,: ICIEA 2019*. IEEE: 505–510. doi:10.1109/ICIEA.2019.8833686.

Goodfellow, Ian, Jean Pouget-Abadie, Mehdi Mirza, Bing Xu, David Warde-Farley, Sherjil Ozair, Aaron Courville, and Yoshua Bengio. 2014. "Generative Adversarial Nets." In *Advances in Neural Information Processing Systems*, edited by Z. Ghahramani, M. Welling, C. Cortes, N. Lawrence, and K. Q. Weinberger. Vol. 27. Curran Associates. Inc.https://proceedings.neurips.cc/paper/2014/file/5ca3e9b122f61f8f06494c97b1afccf3-Paper.pdf.

Gradl, Paul. 2021. "Principles of Directed Energy Deposition for Aerospace Applications." Instructed Course - Drive AM Industry Connect, The University of Texas at El Paso (UTEP), Texas, TX. NASA Marshall Space Flight Center. doi:10.13140/RG.2.2.10504.75527.

Heyrani Nobari, Amin, Wei Chen, and Faez Ahmed. 2021. "*PcDGAN: A Continuous Conditional Diverse Generative*

Adversarial Network for Inverse Design." *Proceedings of the ACM SIGKDD International Conference on Knowledge Discovery and Data Mining* 1. Association for Computing Machinery. doi:10.1145/3447548.3467414.

Huckstepp, Alex. 2019. "Surface Roughness – A Guide to Metal Additive Manufacturing by Digital Alloys – MANUFACTUR3D." https://manufactur3dmag.com/surface-roughness-a-guide-to-metal-additive-manufacturing-by-digital-alloys/.

Jhabvala, Jamasp, Eric Boillat, Thibaud Antignac, and Rémy Glardon. 2010. "On the Effect of Scanning Strategies in the Selective Laser Melting Process." *Virtual and Physical Prototyping* 5 (2): 99–109. doi:10.1080/17452751003688368.

Joshi, Sameehan S., Shashank Sharma, Sangram Mazumder, Mangesh V. Pantawane, and Narendra B. Dahotre. 2021. "Solidification and Microstructure Evolution in Additively Manufactured H13 Steel via Directed Energy Deposition: Integrated Experimental and Computational Approach." *Journal of Manufacturing Processes* 68: 852–866. Elsevier Ltd. doi:10.1016/j.jmapro.2021.06.009.

Keist, Jayme, Karen Taminger, and Todd A. Palmer. 2016. "Structure-Property Correlations for Additively Manufactured Ti-6Al-4V Components Produced Using Directed Energy Deposition Processes." *Proceedings of the 13th World Conference on Titanium*, 1395–1400. doi:10.1002/9781119296126.ch235.

Langebeck, Anika, Annika Bohlen, Rüdiger Rentsch, and Frank Vollertsen. 2020. "Mechanical Properties of High Strength Aluminum Alloy EN AW-7075 Additively Manufactured by Directed Energy Deposition." *Metals*, 1–8.

Lee, Jian Yuan, Arun Prasanth Nagalingam, and S. H. Yeo. 2021. "A Review on the State-of-the-Art of Surface Finishing Processes and Related ISO/ASTM Standards for Metal Additive Manufactured Components." *Virtual and Physical Prototyping* 16 (1): 68–96. Taylor & Francis. doi:10.1080/17452759.2020.1830346.

Li, Boyuan, Han Zheng, Changjun Han, and Kun Zhou. 2021. "Nanotwins-Containing Microstructure and Superior Mechanical Strength of a Cu–9Al–5Fe–5Ni Alloy Additively Manufactured by Laser Metal Deposition." *Additive Manufacturing* 39 (January): 101825. Elsevier B.V. doi:10.1016/j.addma.2020.101825.

Liu, Rui, Sen Liu, and Xiaoli Zhang. 2021. "A Physics-Informed Machine Learning Model for Porosity Analysis in Laser Powder Bed Fusion Additive Manufacturing." *International Journal of Advanced Manufacturing Technology* 113 (7–8): 1943–1958. The International Journal of Advanced Manufacturing Technology. doi:10.1007/s00170-021-06640-3.

Lu, Cuiyuan, Xiaodong Jia, Jay Lee, and Jing Shi. 2022. "Knowledge Transfer Using Bayesian Learning for Predicting the Process-Property Relationship of Inconel Alloys Obtained by Laser Powder Bed Fusion." *Virtual and Physical Prototyping*. no. May. doi:10.1080/17452759.2022.2068447.

Lu, Jinzhong, Haifei Lu, Xiang Xu, Jianhua Yao, Jie Cai, and Kaiyu Luo. 2020. "International Journal of Machine Tools and Manufacture High-Performance Integrated Additive Manufacturing with Laser Shock Peening – Induced Microstructural Evolution and Improvement in Mechanical Properties of Ti6Al4V Alloy Components." *International Journal of Machine Tools and Manufacture* 148 (June 2019): 103475. Elsevier Ltd. doi:10.1016/j.ijmachtools.2019.103475.

Luo, Jia, Jinying Huang, and Hongmei Li. 2021. "A Case Study of Conditional Deep Convolutional Generative Adversarial Networks in Machine Fault Diagnosis." *Journal of Intelligent Manufacturing* 32 (2): 407–425. Springer US. doi:10.1007/s10845-020-01579-w.

Mbodj, Natago Guilé, Mohammad Abuabiah, Peter Plapper, Maxime El Kandaoui, and Slah Yaacoubi. 2021. "Bead Geometry Prediction in Laser-Wire Additive Manufacturing Process Using Machine Learning: Case of Study." *Applied Sciences (Switzerland)* 11: 24. doi:10.3390/app112411949.

Meyers, Sebastian, Miquel Turón Vinãs, Jean Pierre Kruth, Jef Vleugels, and Brecht Van Hooreweder. 2022. "Laser Powder Bed Fusion as a Net-Shaping Method for Reaction Bonded SiC and B4C." *Virtual and Physical Prototyping*. no. May. doi:10.1080/17452759.2022.2077222.

Mozaffar, Mojtaba, Arindam Paul, Reda Al-Bahrani, Sarah Wolff, Alok Choudhary, Ankit Agrawal, Kornel Ehmann, and Jian Cao. 2018. "Data-Driven Prediction of the High-Dimensional Thermal History in Directed Energy Deposition Processes via Recurrent Neural Networks." *Manufacturing Letters* 18: 35–39. Society of Manufacturing Engineers (SME). doi:10.1016/j.mfglet.2018.10.002.

Nam, Sangwoo, Heewon Cho, Cheolhee Kim, and Young Min Kim. 2018. "Effect of Process Parameters on Deposition Properties of Functionally Graded STS 316/Fe Manufactured by Laser Direct Metal Deposition." *Metals* 8: 8. doi:10.3390/met8080607.

Olaf, Engler, and Randle Valerie. 2009. *Introduction to Texture Analysis*. Boca Raton, FL: CRC Press, 21–27. doi:10.1142/9781848161160_0001.

Perarnau, Guim,: Joost Van De Weijer, Bogdan Raducanu, Jose M Álvarez, and Data Csiro. 2016. "Invertible Conditional GANs for Image Editing." doi:10.48550/arXiv.1611.06355.

Perez, Luis, and Jason Wang. 2017. "The Effectiveness of Data Augmentation in Image Classification Using Deep Learning. http://arxiv.org/abs/1712.04621.

Qian, L., J. Mei, J. Liang, and X. Wu. 2005. "Influence of Position and Laser Power on Thermal History and Microstructure of Direct Laser Fabricated Ti-6Al-4V Samples." *Materials Science and Technology* 21 (5): 597–605. doi:10.1179/174328405X21003.

Qiu, Chunlei, G. A. Ravi, Chris Dance, Andrew Ranson, Steve Dilworth, and Moataz M. Attallah. 2015. "Fabrication of Large Ti-6Al-4V Structures by Direct Laser Deposition." *Journal of Alloys and Compounds* 629: 351–361. Elsevier B.V.. doi:10.1016/j.jallcom.2014.12.234.

Radford, Alec, Luke Metz, and Soumith Chintala. 2016. "Unsupervised Representation Learning with Deep Convolutional Generative Adversarial Networks." *4th International Conference on Learning Representations, ICLR 2016 - Conference Track Proceedings*, 1–16.

Rao, Jing, Swee Leong Sing, Joel Choon Wee Lim, Wai Yee Yeong, Jizhong Yang, Zheng Fan, and Paul Hazell. 2022. "Detection and Characterisation of Defects in Directed Energy Deposited Multi-Material Components Using Full Waveform Inversion and Reverse Time Migration." *Virtual and Physical Prototyping*, 1–11. doi:10.1080/17452759.2022.2086142.

Saxena, Divya, and Jiannong Cao. 2020. "Generative Adversarial Networks (GANs): Challenges,: Solutions, and Future Directions." http://arxiv.org/abs/2005.00065.

Shen, M. -H. Herman, and Liang Chen. 2019. "A New CGAN Technique for Constrained Topology Design Optimization." doi:10.48550/arXiv.1901.07675.

Shim, Do Sik, Gyeong Yun Baek, Jin Seon Seo, Gwang Yong Shin, Kee Poong Kim, and Ki Yong Lee. 2016. "Effect of Layer Thickness Setting on Deposition Characteristics in Direct Energy Deposition (DED) Process." *Optics and Laser Technology* 86: 69–78. Elsevier. doi:10.1016/j.optlastec.2016.07.001.

Sridharan, Niyanth, Anil Chaudhary, Peeyush Nandwana, and Sudarsanam Suresh Babu. 2016. "Texture Evolution During Laser Direct Metal Deposition of Ti-6Al-4V." *JOM Journal of the Minerals Metals and Materials Society* 68 (3): 772–777. doi:10.1007/s11837-015-1797-6.

Tandon, Rajiv, Timothy Wilks, Dipl Ing Matthias Gieseke, Dipl Ing Christian Noelke, Stefan Kaierle, and Todd Palmer. 2015. . "Additive Manufacturing of Electron® 43 Alloy Using Laser Powder Bed and Directed Energy Deposition." Proceedings Euro PM 2015: International Power Metallurgy Congress and Exhibition.

Terrassa, Katherine L., Thale R. Smith, Sen Jiang, Joshua D. Sugar, and Julie M. Schoenung. 2019. "Improving Build Quality in Directed Energy Deposition by Cross-Hatching." *Materials Science and Engineering A* 765 (August): 138269. Elsevier B.V.doi:10.1016/j.msea.2019.138269.

Udroiu, Razvan, Ion Cristian Braga, and Anisor Nedelcu. 2019. "Evaluating the Quality Surface Performance of Additive Manufacturing Systems: Methodology and a Material Jetting Case Study." *Materials* 12 (6). doi:10.3390/ma12060995.

Wacker, Christian, Markus Köhler, Martin David, Franziska Aschersleben, Felix Gabriel, Jonas Hensel, Klaus Dilger, and Klaus Dröder. 2021. "Geometry and Distortion Prediction of Multiple Layers for Wire Arc Additive Manufacturing with Artificial Neural Networks." *Applied Sciences (Switzerland)* 11: 10. doi:10.3390/app11104694.

Wang, Zihong, Xin Lin, Nan Kang, Yunlong Hu, Jing Chen, and Weidong Huang. 2020. "Strength-Ductility Synergy of Selective Laser Melted Al-Mg-Sc-Zr Alloy with a Heterogeneous Grain Structure." *Additive Manufacturing* 34 (December 2019): 101260. doi:10.1016/j.addma.2020.101260.

Wang, J. J., Z. X. Wen, X. H. Zhang, Y. C. Zhao, and Z. F. Yue. 2019. "Effect Mechanism and Equivalent Model of Surface Roughness on Fatigue Behavior of Nickel-Based Single Crystal Superalloy." *International Journal of Fatigue* 125 (November 2018): 101–111. Elsevier. doi:10.1016/j.ijfatigue.2019.03.041.

Wang, Jingjing, Wen Jin Wu, Wei Jing, Xipeng Tan, Gui Jun Bi, Shu Beng Tor, Kah Fai Leong, Chee Kai Chua, and Erjia Liu. 2019. "Improvement of Densification and Microstructure of ASTM A131 EH36 Steel Samples Additively Manufactured via Selective Laser Melting with Varying Laser Scanning Speed and Hatch Spacing." *Materials Science and Engineering A* 746 (September 2018): 300–313. Elsevier B.V. doi:10.1016/j.msea.2019.01.019.

Woldesellasse, Haile, and Solomon Tesfamariam. 2022. "Prediction of Lateral Spreading Displacement Using Conditional Generative Adversarial Network (CGAN)." *Soil Dynamics and Earthquake Engineering* 156 (May 2021): 107214. Elsevier Ltd. doi:10.1016/j.soildyn.2022.107214.

Xiao, Xinyi, Clarke Waddell, Carter Hamilton, and Hanbin Xiao. 2022. "Quality Prediction and Control in Wire Arc Additive Manufacturing via Novel Machine Learning Framework." *Micromachines* 13 (1). doi:10.3390/mi13010137.

Xu, Bing, Naiyan Wang, Tianqi Chen, and Mu Li. 2015. "Empirical Evaluation of Rectified Activations in Convolutional Network. http://arxiv.org/abs/1505.00853.

Xue, Pengsheng, Lida Zhu, Jinsheng Ning, Yuan Ren, Zhichao Yang, Shuhao Wang, Peihua Xu, Guiru Meng, Zhe Liu, and Bo Xin. 2021. "Effect of Laser Incident Energy on the Densification and Structure–Property Relationships of Additively Manufactured CrCoNi Medium-Entropy Alloy." *Virtual and Physical Prototyping* 16(4): 404–416. Taylor & Francis. doi:10.1080/17452759.2021.1947509.

Yadollahi, Aref, Nima Shamsaei, Scott M Thompson, Alaa Elwany, and Linkan Bian. 2017. "Effects of Building Orientation and Heat Treatment on Fatigue Behavior of Selective Laser Melted 17-4 PH Stainless Steel." *International Journal of Fatigue* 94: 218–235. Elsevier Ltd. doi:10.1016/j.ijfatigue.2016.03.014.

Yang, Zhichao, Shuhao Wang, Lida Zhu, Jinsheng Ning, Bo Xin, Yichao Dun, and Wentao Yan. 2022. "Manipulating Molten Pool Dynamics During Metal 3D Printing by Ultrasound." *Applied Physics Reviews* 9 (2). American Institute of Physics Inc. doi:10.1063/5.0082461.

Yang, Zhichao, Lida Zhu, Shuhao Wang, Jinsheng Ning, Yichao Dun, Guiru Meng, Pengsheng Xue, Peihua Xu, and Bo Xin. 2021. "Effects of Ultrasound on Multilayer Forming Mechanism of Inconel 718 in Directed Energy Deposition." *Additive Manufacturing* 48 (December). Elsevier B.V. doi:10.1016/j.addma.2021.102462.

Yu, Jun, Marleen Rombouts, Gert Maes, and Filip Motmans. 2012. "Material Properties of Ti-6Al-4v Parts Produced by Laser Metal Deposition." *Physics Procedia* 39: 416–424. doi:10.1016/j.phpro.2012.10.056.

Zhang, Jingzhe, and Ali Fatemi. 2019. "Surface Roughness Effect on Multiaxial Fatigue Behavior of Additive Manufactured Metals and Its Modeling." *Theoretical and Applied Fracture Mechanics* 103 (May): 102260. Elsevier. doi:10.1016/j.tafmec.2019.102260.

Zhang, Yang, Hongyang Jing, Lianyong Xu, Yongdian Han, and Lei Zhao. 2021. "Effects of Different Scanning Patterns on Nickel Alloy-Directed Energy Deposition Based on Thermal Analysis." *Virtual and Physical Prototyping* 16 (S1): S98–S115. doi:10.1080/17452759.2021.1896173. Taylor & Francis.

Zhang, Bo, Di Li, Yan Wang, Zongqing Ma, Xi Wu, Jiliu Zhou, and Luping Zhou. 2021. "LR-CGAN: Latent Representation Based Conditional Generative Adversarial Network for Multi-Modality MRI Synthesis." *Biomedical Signal Processing and Control* 66 (December 2020). doi:10.1016/j.bspc.2021.102457.

Zhang, Jianjing, Peng Wang, and Robert X. Gao. 2018. "Modeling of Layer-Wise Additive Manufacturing for Part Quality Prediction." *Procedia Manufacturing* 16: 155–162. Elsevier B.V. doi:10.1016/j.promfg.2018.10.165.

Zhang, Kai, Shijie Wang, Weijun Liu, and Xiaofeng Shang. 2014. "Characterization of Stainless Steel Parts by Laser Metal Deposition Shaping." *Materials and Design* 55: 104–119. doi:10.1016/j.matdes.2013.09.006. Elsevier Ltd.